AGU ADVANCING EARTH AND SPACE SCIENCES

Geophysical Research Letters®

RESEARCH LETTER
10.1029/2024GL109892

Precipitation Over a Wide Range of Climates Simulated With Comprehensive GCMs

David B. Bonan[1], **Tapio Schneider**[1], **and Jiang Zhu**[2]

[1]Environmental Science and Engineering, California Institute of Technology, Pasadena, CA, USA, [2]Climate and Global Dynamics, NSF National Center for Atmospheric Research, Boulder, CO, USA

Key Points:

- In CAM4, global-mean precipitation increases linearly with surface temperatures up to 330 K, then decreases with higher temperatures
- Precipitation decreases at high temperatures due to increased atmospheric shortwave absorption by water vapor, decreasing surface absorption
- At high temperatures, precipitation decreases in most regions, but continues to increase in the extratropics due to eddy moisture transport

Supporting Information:

Supporting Information may be found in the online version of this article.

Correspondence to:

D. B. Bonan,
dbonan@caltech.edu

Citation:

Bonan, D. B., Schneider, T., & Zhu, J. (2024). Precipitation over a wide range of climates simulated with comprehensive GCMs. *Geophysical Research Letters*, *51*, e2024GL109892. https://doi.org/10.1029/2024GL109892

Received 19 APR 2024
Accepted 6 AUG 2024

Abstract Idealized general circulation models (GCMs) suggest global-mean precipitation ceases to increase with warming in hot climates because evaporation is limited by the available solar radiation at the surface. We investigate the extent to which this generalizes in comprehensive GCMs. We find that in the Community Atmosphere Model, global-mean precipitation increases approximately linearly with global-mean surface temperatures up to about 330 K, where it peaks at 5 mm day^{-1}. Beyond 330 K, global-mean precipitation decreases substantially despite increasing surface temperatures because of increased atmospheric shortwave absorption by water vapor, which decreases the shortwave radiation available for evaporation at the surface. Precipitation decreases in the tropics and subtropics but continues to increase in the extratropics because of continuously strengthening poleward moisture transport. Precipitable water increases everywhere, resulting in longer water-vapor residence times and implying more episodic precipitation. Other GCMs indicate global-mean precipitation might exhibit a smaller maximum rate and begin to decrease at lower surface temperatures.

Plain Language Summary Earth's climate has experienced substantial changes over its history, including periods of extremely cold temperatures where most regions contained ice, and periods of extremely warm temperatures where most regions contained no ice. In this study, we explore how precipitation changed in extremely cold and warm climates using a unique set of coupled climate model simulations. We find that global-mean precipitation increases linearly with global-mean surface temperatures up to 330 K, where it peaks at 5 mm day^{-1} and then decreases as surface temperatures further increase. This occurs because in hot climates, global-mean precipitation is almost entirely balanced by absorbed shortwave radiation at the surface. As the climate warms, the atmosphere contains more water vapor, resulting in increased absorption of shortwave radiation within the atmosphere and decreased absorption of shortwave radiation at the surface. This decreases the energy available for surface evaporation. We show that other climate models exhibit qualitatively similar behavior but indicate global-mean precipitation might exhibit a smaller maximum rate and begin to decrease at lower surface temperatures. These results demonstrate the need to better understand Earth's hydrological cycle in hot climates. These results also have large implications for understanding weathering in past climates and the habitability of other Earth-like planets.

1. Introduction

In the present-day climate, global-mean precipitation is expected to increase at a rate of 1–3% per degree of warming in response to rising greenhouse-gas concentrations (Allen & Ingram, 2002; Held & Soden, 2006; Jeevanjee & Romps, 2018; Pendergrass & Hartmann, 2014; Siler et al., 2019; Vecchi & Soden, 2007). This relationship, often referred to as Earth's global hydrological sensitivity, has been found to be remarkably similar across a variety of greenhouse-gas forcing experiments (Andrews et al., 2010; Andrews & Forster, 2010; DeAngelis et al., 2015; Fläschner et al., 2016; Lambert & Webb, 2008; O'Gorman et al., 2012; Raiter et al., 2023; Stephens & Ellis, 2008). If this relation were to hold across a broad range of climates, it would imply that global-mean precipitation in past climates, such as the early Eocene or the mid-Pliocene, could be inferred directly from paleoclimate temperature records. For example, it is estimated that early Eocene surface temperatures were 12–15 K warmer than the present-day climate (Anagnostou et al., 2016; Caballero & Huber, 2013; Inglis et al., 2020; Zachos et al., 2008), which would suggest that global-mean precipitation would have been 12–45% larger than today.

While the global hydrological sensitivity is a conceptually convenient metric, there is evidence that it varies as a function of climate state, implying that estimates from climates similar to today may not apply to past climates. For instance, O'Gorman and Schneider (2008) simulated a wide range of climates in an idealized GCM and showed that global-mean precipitation levels off with warming in hot climates. Examination of the surface energy budget showed that in hot climates, global-mean precipitation is entirely balanced by absorbed shortwave radiation at the surface, which, in the idealized GCM, is constant because, among other factors, shortwave absorption by water vapor is ignored (O'Gorman & Schneider, 2008). These results suggest that global-mean precipitation may not only level off in hot climates but may even decrease, as increased absorption of shortwave radiation by water vapor may limit the energy available at the surface to evaporate water. However, the idealized GCM employed a simple gray radiation scheme and contained no land, sea ice, or clouds, leaving questions about the behavior of precipitation in comprehensive GCMs.

More recent work examined precipitation in comprehensive GCMs under various atmospheric carbon dioxide (CO_2) levels and found that the global hydrological sensitivity exhibits weak climate state dependence. Good et al. (2012) used a coupled GCM and found that global-mean precipitation is only slightly less sensitive to warming in warm climates. Raiter et al. (2023) examined a broader suite of coupled GCMs and found that the global hydrological sensitivity changes little under large CO_2 forcing. However, these studies did not explore extremely high atmospheric CO_2 concentrations and only simulated a narrow range of Cenozoic Era surface temperatures. Thus, in comprehensive GCMs, it remains unclear whether the global hydrological sensitivity is weaker in hot climates and whether precipitation exhibits significant climate state dependence. Notably, analytical radiative arguments introduced by Jeevanjee and Romps (2018) suggest that in hot climates, precipitation may decrease under warming. Yet, this hypothesis has not been confirmed in comprehensive GCMs, which contain clouds and other processes that can modulate radiative fluxes.

In this study, we examine precipitation over a wide range of climates simulated with comprehensive GCMs. We find that in the Community Atmosphere Model (CAM), global-mean precipitation increases approximately linearly with global-mean surface temperatures up to about 330 K, where it peaks at a rate of approximately 5 mm day^{-1}. Beyond 330 K, global-mean precipitation decreases substantially despite increasing global-mean surface temperatures. The decrease in precipitation indeed occurs because in hot climates, Earth's atmosphere contains more water vapor, resulting in increased absorption of shortwave radiation within the atmosphere and decreased absorption of shortwave radiation at the surface, thereby limiting the energy available for surface evaporation. Other GCMs indicate global-mean precipitation might exhibit a smaller maximum rate and begin to decrease at lower surface temperatures. We also find that extratropical precipitation continues to increase despite decreasing global-mean precipitation because poleward moisture transport continues to strengthen as the climate warms. These results have large implications for understanding Earth's hydrological cycle across various time periods, spanning from the recent past to the Hadean and Archaean eons, as well as for understanding weathering in past climates, and the habitability of other Earth-like planets.

2. Data and Methods

2.1. Climate Model Output

We use simulation output from a suite of comprehensive GCMs that have participated in different phases of the Coupled Model Intercomparison Project. The simulations come from different GCMs and span a wide range of surface temperatures, enabling us to explore the impact of model physics on precipitation as a function of climate state.

2.1.1. Community Atmosphere Model (CAM)

We use a suite of simulations from CAM4, CAM5, and CAM6, which are state-of-the-art atmospheric models within the Community Earth System Model (CESM; Hurrell et al., 2013; Danabasoglu et al., 2020). CAM4 uses different radiative transfer code (Collins et al., 2006) from CAM5 and CAM6, which both use the rapid radiative transfer model for GCMs (Mlawer et al., 1997). CAM4, CAM5, and CAM6 also differ substantially in their physical parameterizations of convection and clouds, leading to different equilibrium climate sensitivities of 3.1 K, 4.2 K, and 5.3 K, respectively (Zhu & Poulsen, 2020b).

Each CAM simulation is performed with a slab-ocean model (SOM) and specified atmospheric CO_2 concentration. The framework is described in more detail by Zhu and Poulsen (2020b). In short, CAM6 simulations were carried out with 1×, 2×, and 4× the preindustrial CO_2 concentration (284.7 ppmv); CAM5 simulations were carried out with 1×, 2×, 4×, and 8× CO_2; and CAM4 simulations were carried out with 1×, 2×, 4×, 8×, 16×, 32×

and 64× CO_2. With CAM4, we perform two additional simulations (128× and 256× CO_2) not described by Zhu and Poulsen (2020b). Note that model instability for CAM6 with 8×CO_2 and CAM5 with 16×CO_2 prevented higher CO_2 simulations. Each simulation uses identical non-CO_2 boundary conditions, including mixed layer depths and ocean heat transport convergence derived from corresponding fully coupled preindustrial simulations with a dynamic ocean. All CAM4 and CAM5 simulations were run with a horizontal resolution of 1.9° × 2.5° (latitude × longitude) for 60 model years, except for the CAM4 64×, 128×, and 256×CO_2 simulations, which were run for 80 model years. All CAM6 simulations were run for 80 model years. The last 20 years of each simulation were used to calculate climatologies. The global-mean surface temperature range covered by these simulations is broadly comparable to paleoclimate temperatures over the Cenozoic Era and beyond.

We also use a suite of climate simulations that are described in more detail by Wolf et al. (2018). These simulations use a modified version of CAM4 with a SOM and a horizontal resolution of 4° × 5°. The modified version of CAM4 uses a correlated-k radiative transfer model to accurately simulate extremely warm climates (Wolf & Toon, 2013). We use 22 simulations with atmospheric CO_2 concentrations starting from 1.40625 ppmv and doubling until 2,949,120 ppmv.

While CAM4 is less advanced than CAM5 and CAM6, it is still a comprehensive atmospheric model with more sophisticated parameterizations compared to the idealized gray-radiation model used in O'Gorman and Schneider (2008).

2.1.2. LongRunMIP

We use a set of simulations from LongRunMIP (Rugenstein et al., 2019), which is a model intercomparison project that aims to better understand centennial and millennial time scale atmosphere-ocean processes in comprehensive, coupled GCMs. We use all GCMs that provide a preindustrial control simulation and 2×, 4×, 8×, and 16× CO_2. There are no simulations with higher CO_2 forcing. We assume that each preindustrial control simulation has an atmospheric CO_2 concentration of 284.7 ppmv. For all simulations, except those from CNRM-CM6-1, we average each variable over years 971–1,000. For the CNRM-CM6-1 simulations, we average over years 721–750 as this is the longest available time period after 2×CO_2. Most simulations have little-to-no global-mean ocean heat uptake and are therefore close to equilibrium at this time period.

2.2. Energy Budget Diagnostics

2.2.1. Global

Global-mean precipitation can be examined through the surface energy budget. The global-mean (denoted by an overbar) surface energy budget can be expressed as

$$0 = \bar{S} - \bar{L} - L_v\bar{E} - \bar{H} - \bar{G}, \tag{1}$$

where S is the net downward shortwave flux, L is the net upward longwave flux, E is the surface evaporation flux, L_v is the latent heat of vapourization, H is the sensible heat flux from the surface into the atmosphere, and G is ocean heat uptake. On interannual and longer timescales, $\bar{E}$ is equal to precipitation $\bar{P}$, which results in

$$\bar{P} \equiv \bar{E} = \frac{1}{L_v}(\bar{S} - \bar{L} - \bar{H} - \bar{G}). \tag{2}$$

The radiative fluxes S and L can be further decomposed into clear-sky (clr) and cloud components (cld) such that $S = S_{clr} + S_{cld}$ and $L = L_{clr} + L_{cld}$. For the CAM simulations, we decompose S and L into clear-sky and cloud components, while for the LongRunMIP simulations, we cannot decompose S and L due to the lack of clear-sky surface flux output.

O'Gorman and Schneider (2008) showed that Equation 2 can explain the structure of global-mean precipitation as a function of climate state, including the processes controlling the maximum rate of precipitation in hot climates.

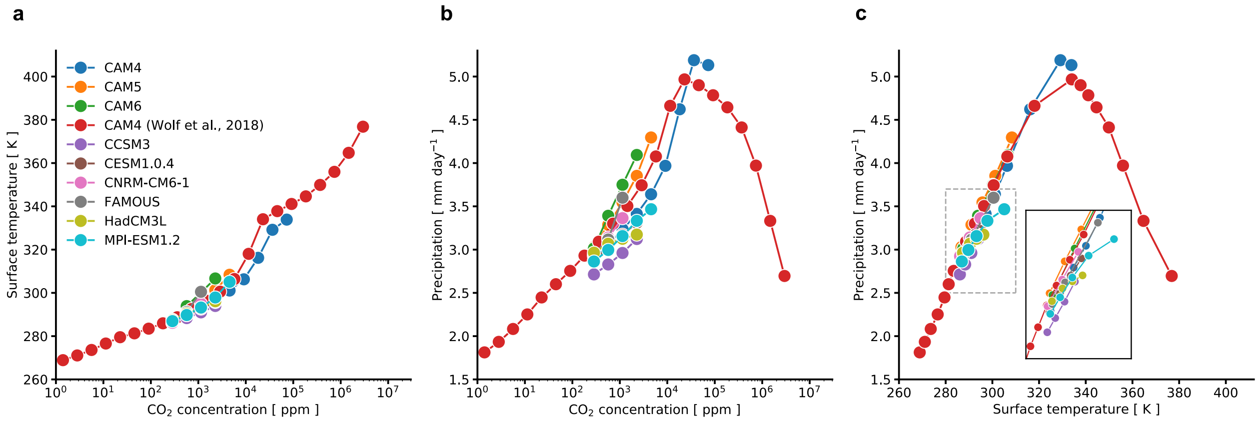

Figure 1. Global-mean precipitation over a wide range of climates. (a) Global-mean surface temperature (K) as a function of the atmospheric CO_2 concentration for the CAM slab-ocean model simulations and fully coupled LongRunMIP simulations. (b) Same as in (a) but for global-mean precipitation (mm day^{-1}). (c) Same as in (b) but for global-mean precipitation as a function of global-mean surface temperature. The inset in (c) shows an enlarged version of the gray dashed box.

2.2.2. Regional

Regional precipitation can also be examined through the surface energy budget with the addition of the latent energy flux divergence $\nabla \cdot F_{\text{latent}}$. On long time scales,

$$P - E = -\frac{1}{L_v}\nabla \cdot F_{\text{latent}}, \tag{3}$$

which means that, using the surface energy budget, regional precipitation can be expressed as

$$P = \frac{1}{L_v}(S - L - H - G - \nabla \cdot F_{\text{latent}}). \tag{4}$$

We examine regional precipitation through the surface energy budget as it connects directly to our approach for global-mean precipitation and provides a physically intuitive understanding of energetic constraints on evaporation, which is how moisture enters the atmosphere. Note that integrating Equation 4 globally results in exactly Equation 2. Global and regional precipitation can also be examined through the atmospheric energy budget (e.g., Bonan, Feldl, et al., 2023; Muller & O'Gorman, 2011; O'Gorman et al., 2012; Pendergrass & Hartmann, 2014).

3. Precipitation Over a Wide Range of Climates

3.1. Global-Mean Precipitation

We begin by examining global-mean precipitation as a function of atmospheric CO_2 concentration and global-mean surface temperature (Figure 1). Under high CO_2 concentrations, GCMs exhibit large intermodel differences in global-mean surface temperatures (Figure 1a). For example, across GCMs, global-mean surface temperatures for CO_2 concentrations near 1,000 ppmv range from 289 to 300 K. While the intermodel spread in surface temperatures is large, these simulations, with the exception of CAM4 (blue and red lines, Figure 1a), only span a small range of Cenezoic Era paleoclimate temperatures. The two versions of CAM4 with different radiation schemes simulate an even larger range of global-mean surface temperatures, ranging from 265 to 380 K (blue and red lines, Figure 1a). Note the nonlinear relationship between carbon-dioxide and surface temperature in these simulations indicate that Earth's climate sensitivity exhibits considerable state dependence for global-mean surface temperatures around 310 K, which has been noted in several other studies (e.g., Caballero & Huber, 2013; Henry et al., 2023; Seeley & Jeevanjee, 2021; Wolf et al., 2018; Zhu & Poulsen, 2020b).

GCMs also exhibit a large intermodel spread in global-mean precipitation as a function of atmospheric CO_2 concentration (Figure 1b). For example, across GCMs, global-mean precipitation for CO_2 concentrations near 1,000 ppmv ranges from approximately 2.8 mm day^{-1} to approximately 4.0 mm day^{-1}. Interestingly, for CO_2 concentrations beyond 30,000 ppmv, the CAM4 simulations indicate that global-mean precipitation decreases

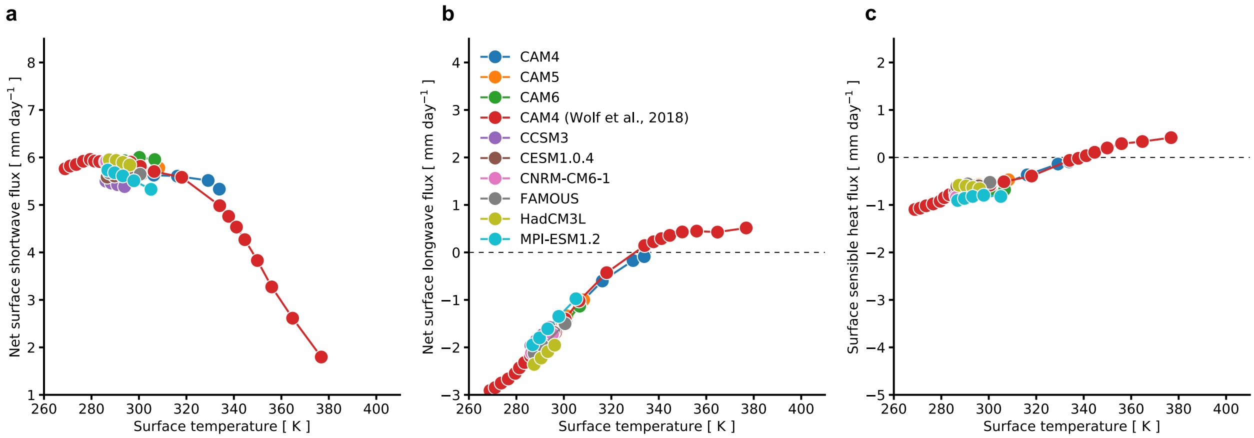

Figure 2. Contributions to global-mean precipitation over a wide range of climates. The global-mean (a) net surface shortwave flux, (b) net surface longwave flux, and (c) surface sensible heat flux as a function of global-mean surface temperature for the CAM slab-ocean model simulations and fully coupled LongRunMIP simulations. Ocean heat uptake is near-zero for all simulations and is not shown.

(Figure 1b) despite surface temperature increases (Figure 1a). Both versions of CAM4 exhibit a global-mean precipitation decrease, despite having different radiation codes (blue and red lines, Figure 1b).

These results can be further understood by plotting global-mean precipitation as a function of global-mean surface temperature; the derivative of this function is the global hydrological sensitivity (Figure 1c). From cold (~270 K) to warm (~320 K) climates, global-mean precipitation exhibits a fairly linear relationship with global-mean surface temperature, with only slight decreases in the rate of global-mean precipitation increase. In hot (>320 K) climates, the CAM4 simulations indicate that global-mean precipitation increases more slowly with global-mean surface temperature and eventually decreases at approximately 330 K (Figure 1c). In the CAM4 simulations from Wolf et al. (2018), which contain more accurate radiation code, global-mean precipitation continues to decrease substantially despite increasing surface temperatures. Note that other GCMs, such as MPI-ESM1.2 and HadCM3L, exhibit overall weaker increases in precipitation for the same surface temperature range as the CAM simulations (gold and light blue lines, Figure 1c). This indicates that global-mean precipitation might exhibit a smaller maximum rate and could begin to decrease at lower surface temperatures.

To understand the mechanisms contributing to global-mean precipitation as a function of global-mean surface temperature, we examine the surface energy budget (see Section 2.2.1). Figure 2 shows the components of the surface energy budget (converted from W m^{-2} to mm day^{-1}). The clear-sky and cloud components of the net surface shortwave and net surface longwave fluxes are shown in Figure S1 in Supporting Information S1.

From cold to warm climates, the global-mean net surface shortwave flux exhibits relatively little change, though there is large intermodel spread (Figure 2a). For example, the CAM simulations exhibit little change in the net surface shortwave flux, whereas MPI-ESM1.2 exhibits a strong decrease. From cold to warm climates, both the net surface longwave flux and surface sensible heat flux approach zero with little intermodel spread (Figures 2b and 2c). The net surface longwave flux change is almost entirely driven by the clear-sky component (Figure S1 in Supporting Information S1).

In hot climates, the net surface longwave flux and surface sensible heat flux are zero or slightly positive (Figures 2b and 2c). This occurs because differences in surface and tropospheric air temperatures become small, and the atmosphere approaches the optically thick limit, where upward longwave emission at the surface and the downward longwave emission from within the atmosphere that reaches the surface occur at almost the same temperature (O'Gorman & Schneider, 2008). As a result, global-mean evaporation, and thus global-mean precipitation, is almost entirely balanced by the net surface shortwave flux, which exhibits a strong decrease in hot climates (Figure 2a). The clear-sky component of the net surface shortwave flux decreases in hot climates (Figure S1 in Supporting Information S1) because of increased shortwave absorption by the atmosphere due to water vapor (Figure S2 in Supporting Information S1). The decrease in net surface shortwave flux occurs in both CAM4 simulations, though the decrease is stronger at high temperatures in the CAM4 simulations from Wolf et al. (2018) (blue and red lines, Figure 2a).

3.2. Zonal-Mean Precipitation

We now examine zonal-mean precipitation as a function of global-mean surface temperature (Figure 3). We focus on the CAM simulations to understand the regions contributing to the decrease in global-mean precipitation for surface temperatures beyond 330 K. The same analysis for each simulation from LongRunMIP is shown in Figure S3 in Supporting Information S1.

From cold to warm climates, precipitation increases in most regions, with substantial increases in the tropics and extratropics and small decreases in the subtropics (Figure 3a). In hot climates (>320 K), subtropical and tropical precipitation decreases substantially. The maximum tropical precipitation is approximately 10 mm day^{-1} in warm climates and decreases to approximately 5 mm day^{-1} in hot climates. Similarly, subtropical precipitation decreases from approximately 6 mm day^{-1} in warm climates to approximately 0 mm day^{-1} in hot climates. Notably, from warm to hot climates, despite a decrease in global-mean precipitation, precipitation continues to increase in the extratropics, with the polar regions experiencing a substantial increase in precipitation (Figure 3a). Precipitation in the Arctic, for instance, increases from approximately 2 mm day^{-1} in warm climates to approximately 8 mm day^{-1} in hot climates.

To understand the mechanisms contributing to regional precipitation as a function of global-mean surface temperature, we examine components of the surface energy budget and latent energy flux divergence (see Section 2.2.2). Figures 3b–3e show the components of the zonal-mean surface energy budget and latent energy flux divergence (converted from W m^{-2} to mm day^{-1}) for the CAM simulations.

From cold to warm climates, the net surface shortwave flux remains relatively constant, exhibiting weak increases in the polar regions (Figure 3b). Figure S4 in Supporting Information S1 shows the clear-sky and cloud components of the zonal-mean net surface shortwave flux and shows that this is related mainly to the clear-sky component. The overall increase in zonal-mean precipitation from cold to warm climates is contributed mainly by the net surface longwave flux, which becomes smaller under warming (Figure 3c). The surface sensible heat flux contributes weakly to the overall increase in zonal-mean precipitation from cold to warm climates (Figure 3d). The latent energy flux divergence contributes most to the zonal-mean pattern of precipitation, causing a precipitation increase in the tropics and extratropics, and a precipitation decrease in the subtropics (Figure 3e). Note there are substantial changes in the latent energy flux divergence around 320 K that indicate meridional shifts in tropical rainfall, expansion of the subtropics, and poleward shifts of the midlatitude stormtracks.

In hot climates (>320 K), the net surface longwave flux and surface sensible heat flux become much smaller and approach zero (Figures 3c and 3d). As a result, in hot climates, regional precipitation is almost entirely balanced by the net surface shortwave flux and latent energy flux divergence (Figures 3b and 3e). In the subtropics, the weak export of moisture associated with increased poleward latent energy transport (Figure 3e) is balanced almost entirely by the net surface shortwave flux, resulting in no precipitation (Figure 3a). Note that the subtropics continue to see drying in extremely hot climates, largely due to the increased latent energy transport (Figure 3e). In the extratropics, precipitation continues to increase in hot climates because of increased poleward latent energy transport. In the polar regions, the decrease in net surface shortwave flux is small (Figure 3b), but the increase in poleward latent energy transport is large (Figure 3e), resulting in a overall precipitation increase (Figure 3a).

3.3. Total Precipitable Water and Precipitation Intensity

The decrease in global-mean precipitation for surface temperatures above 330 K has important implications for precipitation intensity and precipitation extremes. Scaling arguments and simulations suggest that precipitation extremes depend primarily on the atmospheric water vapor content (O'Gorman & Schneider, 2009a, 2009b), which should continue to increase with warming (O'Gorman & Schneider, 2008). A decrease in global-mean precipitation but increase in global-mean atmospheric water vapor content implies that precipitation would have to become more episodic and potentially more intense.

Due to the lack of high-frequency temporal output, we are unable to quantitatively examine precipitation extremes (e.g., O'Gorman & Schneider, 2009a, 2009b). However, we can examine the total precipitable water and calculate the water vapor residence time, defined as the global-mean total precipitable water divided by the global-mean

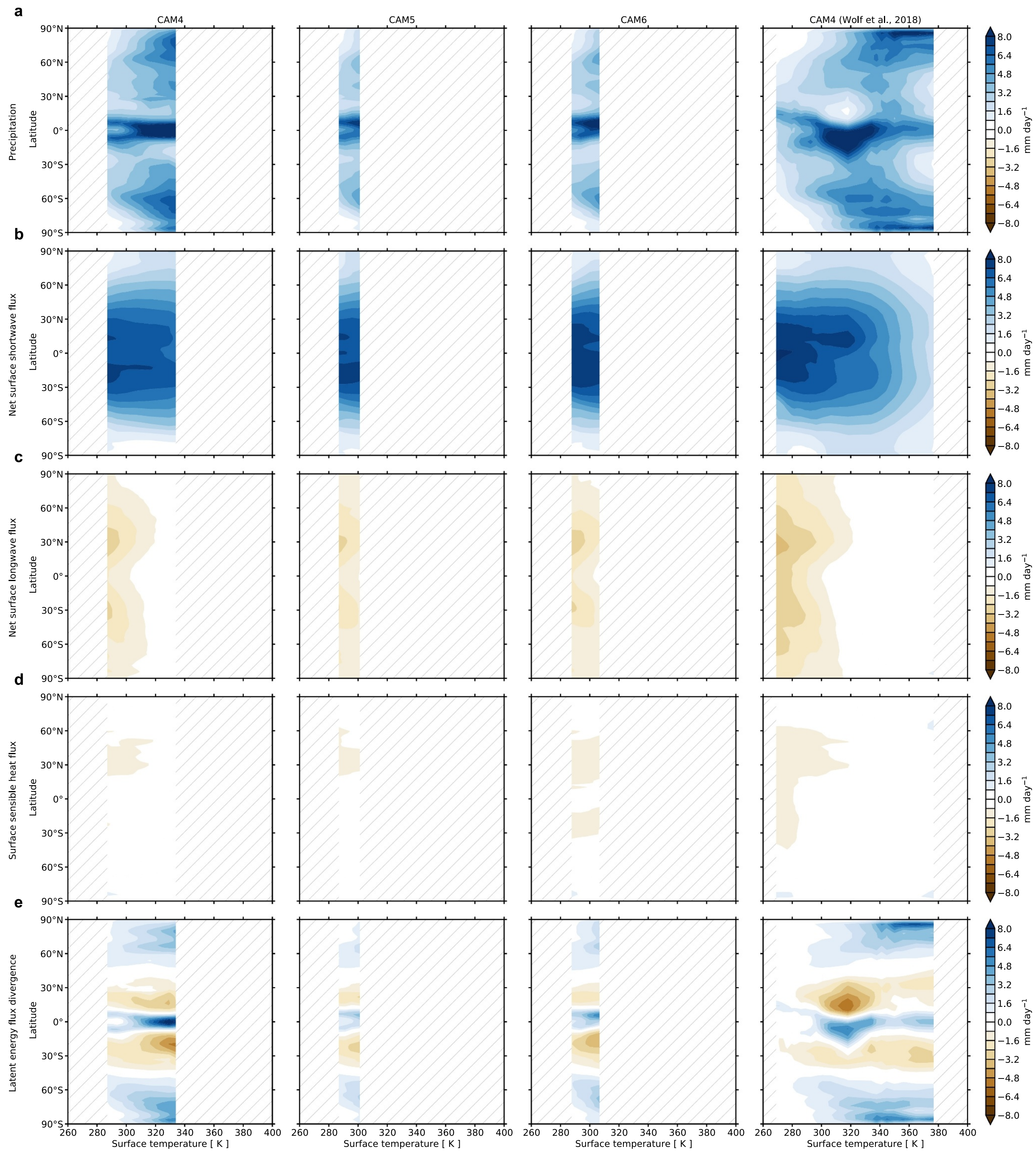

Figure 3. Zonal-mean precipitation over a wide range of climates. (a) The zonal-mean precipitation as a function of global-mean surface temperature for the CAM4, CAM5, and CAM6 simulations. The zonal-mean (b) net surface shortwave flux, (c) net surface longwave flux, (d) surface sensible heat flux, and (e) latent energy flux divergence (converted from W m^{-2} to mm day^{-1}) as a function of global-mean surface temperature for the CAM4, CAM5, and CAM6 simulations. Ocean heat uptake is zero for all simulations and is not shown. Panels (b)–(e) add to panel (a). The light gray hatching indicates no simulation data.

precipitation (Bosilovich et al., 2005; Trenberth, 1998). The water vapor residence time can help indicate precipitation intensity. For instance, a climate with the same mean precipitation as today but a longer water vapor residence time implies there is more episodic and intense precipitation.

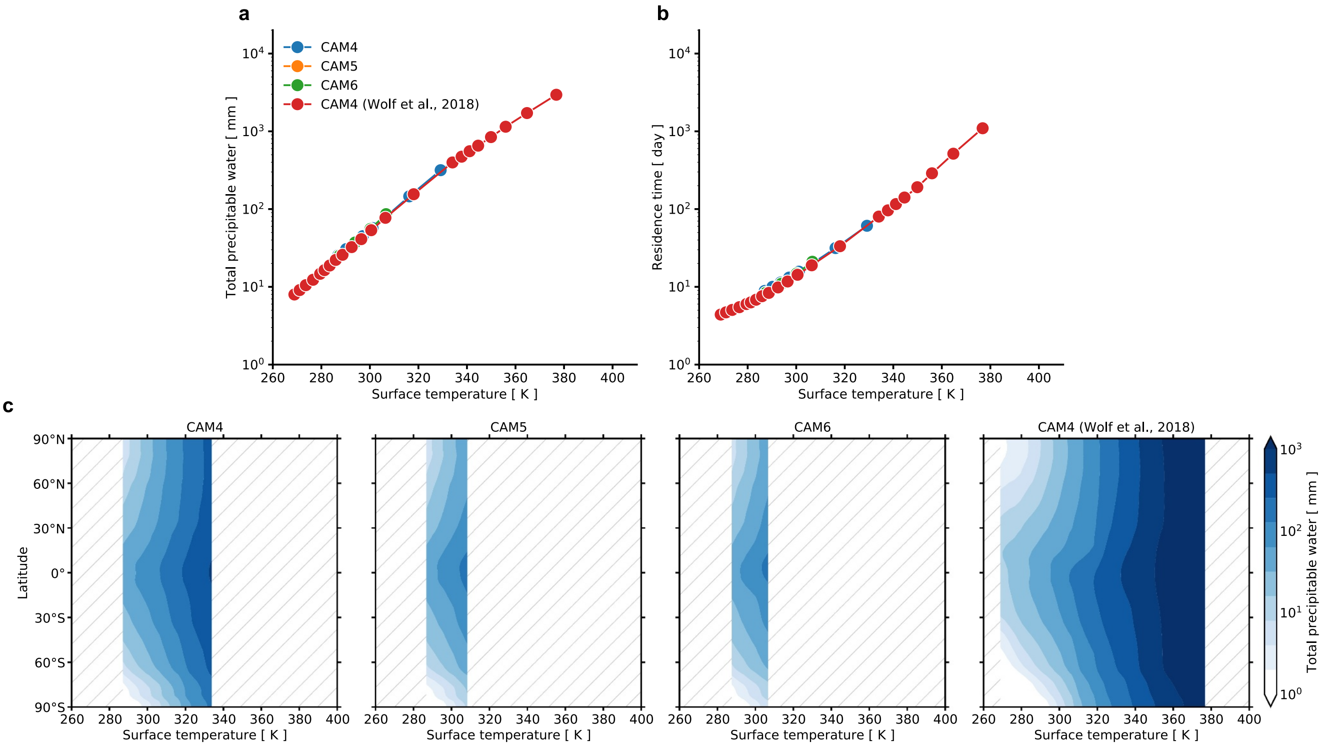

Figure 4. Residence time of water vapor over a wide range of climates. The global-mean (a) total precipitable water and (b) residence time of water vapor for the CAM4, CAM5, and CAM6 simulations. (c) Zonal-mean total precipitable water as a function of global-mean surface temperature for the CAM4, CAM5, and CAM6 simulations. The light gray hatching indicates no simulation data.

The global-mean total precipitable water (Figure 4a) and global-mean water vapor residence time (Figure 4b) increase with increasing global-mean surface temperatures. From cold to warm climates, total precipitable water increases at a rate of 6–7% K^{-1} and the water vapor residence time increases at a rate of 4–5% K^{-1}. In hot climates, the total precipitable water continues to increase (Figure 4a), resulting in a global-mean water vapor residence time of approximately 1 yr at 350 K (Figure 4b). The total precipitable water increases most in the tropics and subtropics (Figure 4c), which likely results in regional variations of precipitation intensity. For climates between 320 and 330 K, precipitation is likely more intense and episodic due to the relatively similar global-mean precipitation (Figure 1c) but increase in water vapor residence time (Figure 4b).

4. Discussion and Conclusions

In this study, we examined precipitation over a wide range of climates simulated with comprehensive GCMs. Building on earlier work by O'Gorman and Schneider (2008), we showed that global-mean precipitation increases approximately linearly with global-mean surface temperatures from cold to warm climates and begins to increase more slowly in hot climates (Figure 1c)—consistent with Good et al. (2012). However, in contrast to these studies, we found that, at least for CAM4, global-mean precipitation decreases substantially after 330 K, despite increasing surface temperatures (Figure 1c). This occurs because global-mean precipitation is almost entirely balanced by the absorbed shortwave radiation at the surface in hot climates (Figure 2). As the climate warms, Earth's atmosphere contains more water vapor, resulting in increased absorption of shortwave radiation within the atmosphere and decreased absorption of shortwave radiation at the surface (Figure 2a and Figure S2 in Supporting Information S1). This decreases the energy available for surface evaporation and causes a decrease in global-mean precipitation with further warming. These results are consistent with the analysis of O'Gorman and Schneider (2008) and the analytical radiative arguments of Jeevanjee and Romps (2018). Similar results showing a decrease in global-mean precipitation in hot climates were independently found by Liu et al. (2024) during the review process.

The decrease in global-mean precipitation in CAM4 for surface temperatures beyond 330 K is driven by a decrease in tropical and subtropical precipitation (Figure 3a). Extratropical precipitation continues to increase, despite a decrease in global-mean precipitation (Figure 3a). This occurs because of increases in poleward latent energy transport (Figure 3e), which is a well-known feature of hot climates (Caballero & Langen, 2005; O'Gorman & Schneider, 2008). However, the increase in poleward latent energy transport exhibits significant deviations from the increase expected solely from the Clausius-Clapeyron relation (Held & Soden, 2006). These deviations include meridional shifts in tropical rainfall, expansions and contractions of the subtropical regions, and poleward migrations of the extratropical storm tracks. A series of studies have shown that a one-dimensional moist energy balance model can accurately simulate poleward moisture transport in comprehensive GCMs (Armour et al., 2019; Bonan et al., 2024; Bonan, Siler, et al., 2023; Siler et al., 2018), suggesting that down-gradient energy transport might explain the range of poleward latent transport seen in CAM4, including dynamical changes associated with the Hadley circulations.

While our results show considerable climate state dependence in precipitation, the simulations used are driven purely by changes in atmospheric CO_2 concentrations and do not contain changes in other boundary conditions that impact hot climates (see review by Zhu et al., 2024). For example, the early Eocene experienced significant changes in orbital dynamics (Lourens et al., 2005) as well as in continental land configurations and ocean circulation (Barron, 1987; Green & Huber, 2013; Shellito et al., 2009), each of which could potentially alter the surface energy budget. Examining the effect of other forcings on precipitation in hot climates might change these results.

Despite this caveat, our work has implications for other aspects of Earth's hydrological cycle. We showed that global-mean total precipitable water increases more strongly with warming when compared to global-mean precipitation (Figures 4a and 1c), which results in a longer global-mean water vapor residence time (Figure 4b). Thus, precipitation would have to become more episodic at high surface temperatures. However, due to the lack of higher-frequency output we are unable to quantitatively examine precipitation intensity and precipitation extremes. Note that recent work showed precipitation in hot climates is indeed more episodic and occurs in short and intense outbursts separated by multi-day dry spells (Dagan et al., 2023; Seeley & Wordsworth, 2021). However, these studies employed an idealized cloud-resolving model with limited domains. It remains unclear what episodic precipitation looks like in hot climates simulated with comprehensive GCMs. Future work should explore other characteristics of precipitation in hot climates. Such work will help to better understand mechanisms for hydrological change in past and future climates.

Overall, our results show that precipitation is strongly dependent on the climate state. While the CAM simulations indicate that global-mean precipitation exhibits a maximum rate of approximately 5 mm day^{-1} and decreasing rates for surface temperatures beyond 330 K, other GCMs, like HadCM3L and MPI-ESM1.2, indicate that global-mean precipitation might exhibit a smaller maximum rate and begin to decrease at lower surface temperatures. These differences are attributable to shortwave radiation and may be related to water vapor absorption parameterizations, which vary considerably across comprehensive GCMs (e.g., Fildier & Collins, 2015; Kim et al., 2022; Takahashi, 2009; Yang et al., 2016). Hence, there is a need to examine Earth's hydrological cycle in hot climates simulated with a broader suite of comprehensive GCMs. Such work will have large implications for understanding various climate time periods, spanning from the recent past to the Hadean and Archaean eons, as well as for understanding weathering in past climates, and the habitability of other Earth-like planets.

Data Availability Statement

CAM4, CAM5, and CAM6 output is available in the Zenodo repository via Zhu and Poulsen (2020a). LongRunMIP output is freely available at http://www.longrunmip.org/. The CAM4 output with modified radiation is available at: https://archive.org/download/EvaluatingClimateSensitivityToCO2AcrossEarthsHistory_201809.

Acknowledgments

The authors thank Thorsten Mauritsen for helpful comments during the early stages of this research. D.B.B was supported by the National Science Foundation (NSF) Graduate Research Fellowship Program (NSF Grant DGE1745301). T.S. was supported by Schmidt Sciences, LLC. This material is based upon work supported by the National Center for Atmospheric Research (NCAR), which is a major facility sponsored by the NSF under Cooperative Agreement 1852977.

References

Allen, M. R., & Ingram, W. J. (2002). Constraints on future changes in climate and the hydrologic cycle. *Nature*, *419*(6903), 224–232. https://doi.org/10.1038/nature01092

Anagnostou, E., John, E. H., Edgar, K. M., Foster, G. L., Ridgwell, A., Inglis, G. N., et al. (2016). Changing atmospheric CO2 concentration was the primary driver of early Cenozoic climate. *Nature*, *533*(7603), 380–384. https://doi.org/10.1038/nature17423

Andrews, T., & Forster, P. M. (2010). The transient response of global-mean precipitation to increasing carbon dioxide levels. *Environmental Research Letters*, *5*(2), 025212. https://doi.org/10.1088/1748-9326/5/2/025212

Andrews, T., Forster, P. M., Boucher, O., Bellouin, N., & Jones, A. (2010). Precipitation, radiative forcing and global temperature change. *Geophysical Research Letters*, *37*(14). https://doi.org/10.1029/2010gl043991

Armour, K. C., Siler, N., Donohoe, A., & Roe, G. H. (2019). Meridional atmospheric heat transport constrained by energetics and mediated by large-scale diffusion. *Journal of Climate*, *32*(12), 3655–3680. https://doi.org/10.1175/jcli-d-18-0563.1

Barron, E. J. (1987). Eocene equator-to-pole surface ocean temperatures: A significant climate problem? *Paleoceanography*, *2*(6), 729–739. https://doi.org/10.1029/pa002i006p00729

Bonan, D. B., Feldl, N., Siler, N., Kay, J. E., Armour, K. C., Eisenman, I., & Roe, G. H. (2024). The influence of climate feedbacks on regional hydrological changes under global warming. *Geophysical Research Letters*, *51*(3), e2023GL106648. https://doi.org/10.1029/2023gl106648

Bonan, D. B., Feldl, N., Zelinka, M. D., & Hahn, L. C. (2023). Contributions to regional precipitation change and its polar-amplified pattern under warming. *Environmental Research: Climate*, *2*(3), 035010. https://doi.org/10.1088/2752-5295/ace27a

Bonan, D. B., Siler, N., Roe, G. H., & Armour, K. C. (2023). Energetic constraints on the pattern of changes to the hydrological cycle under global warming. *Journal of Climate*, *36*(10), 3499–3522. https://doi.org/10.1175/jcli-d-22-0337.1

Bosilovich, M. G., Schubert, S. D., & Walker, G. K. (2005). Global changes of the water cycle intensity. *Journal of Climate*, *18*(10), 1591–1608. https://doi.org/10.1175/jcli3357.1

Caballero, R., & Huber, M. (2013). State-dependent climate sensitivity in past warm climates and its implications for future climate projections. *Proceedings of the National Academy of Sciences*, *110*(35), 14162–14167. https://doi.org/10.1073/pnas.1303365110

Caballero, R., & Langen, P. L. (2005). The dynamic range of poleward energy transport in an atmospheric general circulation model. *Geophysical Research Letters*, *32*(2). https://doi.org/10.1029/2004gl021581

Collins, W. D., Bitz, C. M., Blackmon, M. L., Bonan, G. B., Bretherton, C. S., Carton, J. A., et al. (2006). The community climate system model version 3 (CCSM3). *Journal of Climate*, *19*(11), 2122–2143. https://doi.org/10.1175/jcli3761.1

Dagan, G., Seeley, J. T., & Steiger, N. (2023). Convection and convective-organization in hothouse climates. *Journal of Advances in Modeling Earth Systems*, *15*(11), e2023MS003765. https://doi.org/10.1029/2023ms003765

Danabasoglu, G., Lamarque, J.-F., Bacmeister, J., Bailey, D., DuVivier, A., Edwards, J., et al. (2020). The community earth system model version 2 (CESM2). *Journal of Advances in Modeling Earth Systems*, *12*(2), e2019MS001916. https://doi.org/10.1029/2019ms001916

DeAngelis, A. M., Qu, X., Zelinka, M. D., & Hall, A. (2015). An observational radiative constraint on hydrologic cycle intensification. *Nature*, *528*(7581), 249–253. https://doi.org/10.1038/nature15770

Fildier, B., & Collins, W. D. (2015). Origins of climate model discrepancies in atmospheric shortwave absorption and global precipitation changes. *Geophysical Research Letters*, *42*(20), 8749–8757. https://doi.org/10.1002/2015gl065931

Fläschner, D., Mauritsen, T., & Stevens, B. (2016). Understanding the intermodel spread in global-mean hydrological sensitivity. *Journal of Climate*, *29*(2), 801–817. https://doi.org/10.1175/jcli-d-15-0351.1

Good, P., Ingram, W., Lambert, F. H., Lowe, J. A., Gregory, J. M., Webb, M. J., et al. (2012). A step-response approach for predicting and understanding non-linear precipitation changes. *Climate Dynamics*, *39*(12), 2789–2803. https://doi.org/10.1007/s00382-012-1571-1

Green, J., & Huber, M. (2013). Tidal dissipation in the early Eocene and implications for ocean mixing. *Geophysical Research Letters*, *40*(11), 2707–2713. https://doi.org/10.1002/grl.50510

Held, I. M., & Soden, B. J. (2006). Robust responses of the hydrological cycle to global warming. *Journal of Climate*, *19*(21), 5686–5699. https://doi.org/10.1175/jcli3990.1

Henry, M., Vallis, G. K., Lutsko, N. J., Seeley, J. T., & McKim, B. A. (2023). State-dependence of the equilibrium climate sensitivity in a clear-sky GCM. *Geophysical Research Letters*, *50*(23), e2023GL104413. https://doi.org/10.1029/2023gl104413

Hurrell, J. W., Holland, M. M., Gent, P. R., Ghan, S., Kay, J. E., Kushner, P. J., et al. (2013). The community earth system model: A framework for collaborative research. *Bulletin of the American Meteorological Society*, *94*(9), 1339–1360. https://doi.org/10.1175/bams-d-12-00121.1

Inglis, G. N., Bragg, F., Burls, N., Evans, D., Foster, G. L., Huber, M., et al. (2020). Global mean surface temperature and climate sensitivity of the EECO, PETM and latest Paleocene. *Climate of the Past Discussions*, *2020*, 1–43.

Jeevanjee, N., & Romps, D. M. (2018). Mean precipitation change from a deepening troposphere. *Proceedings of the National Academy of Sciences*, *115*(45), 11465–11470. https://doi.org/10.1073/pnas.1720683115

Kim, H., Pendergrass, A. G., & Kang, S. M. (2022). The dependence of mean climate state on shortwave absorption by water vapor. *Journal of Climate*, *35*(7), 2189–2207. https://doi.org/10.1175/jcli-d-21-0417.1

Lambert, F. H., & Webb, M. J. (2008). Dependency of global mean precipitation on surface temperature. *Geophysical Research Letters*, *35*(16). https://doi.org/10.1029/2008gl034838

Liu, J., Yang, J., Ding, F., Chen, G., & Hu, Y. (2024). Hydrologic cycle weakening in hothouse climates. *Science Advances*, *10*(17), eado2515. https://doi.org/10.1126/sciadv.ado2515

Lourens, L. J., Sluijs, A., Kroon, D., Zachos, J. C., Thomas, E., Röhl, U., et al. (2005). Astronomical pacing of late Palaeocene to early Eocene global warming events. *Nature*, *435*(7045), 1083–1087. https://doi.org/10.1038/nature03814

Mlawer, E. J., Taubman, S. J., Brown, P. D., Iacono, M. J., & Clough, S. A. (1997). Radiative transfer for inhomogeneous atmospheres: RRTM, a validated correlated-k model for the longwave. *Journal of Geophysical Research*, *102*(D14), 16663–16682. https://doi.org/10.1029/97jd00237

Muller, C. J., & O'Gorman, P. (2011). An energetic perspective on the regional response of precipitation to climate change. *Nature Climate Change*, *1*(5), 266–271. https://doi.org/10.1038/nclimate1169

O'Gorman, P. A., Allan, R. P., Byrne, M. P., & Previdi, M. (2012). Energetic constraints on precipitation under climate change. *Surveys in Geophysics*, *33*(3–4), 585–608. https://doi.org/10.1007/s10712-011-9159-6

O'Gorman, P. A., & Schneider, T. (2008). The hydrological cycle over a wide range of climates simulated with an idealized GCM. *Journal of Climate*, *21*(15), 3815–3832. https://doi.org/10.1175/2007jcli2065.1

O'Gorman, P. A., & Schneider, T. (2009a). The physical basis for increases in precipitation extremes in simulations of 21st-century climate change. *Proceedings of the National Academy of Sciences*, *106*(35), 14773–14777. https://doi.org/10.1073/pnas.0907610106

O'Gorman, P. A., & Schneider, T. (2009b). Scaling of precipitation extremes over a wide range of climates simulated with an idealized GCM. *Journal of Climate*, *22*(21), 5676–5685. https://doi.org/10.1175/2009jcli2701.1

Pendergrass, A. G., & Hartmann, D. L. (2014). The atmospheric energy constraint on global-mean precipitation change. *Journal of Climate*, *27*(2), 757–768. https://doi.org/10.1175/jcli-d-13-00163.1

Raiter, D., Polvani, L. M., Mitevski, I., Pendergrass, A. G., & Orbe, C. (2023). Little change in apparent hydrological sensitivity at large CO2 forcing. *Geophysical Research Letters*, *50*(18), e2023GL104954. https://doi.org/10.1029/2023gl104954

Rugenstein, M., Bloch-Johnson, J., Abe-Ouchi, A., Andrews, T., Beyerle, U., Cao, L., et al. (2019). LongRunMIP: Motivation and design for a large collection of millennial-length AOGCM simulations. *Bulletin of the American Meteorological Society*, *100*(12), 2551–2570. https://doi.org/10.1175/bams-d-19-0068.1

Seeley, J. T., & Jeevanjee, N. (2021). H2O windows and CO2 radiator fins: A clear-sky explanation for the peak in equilibrium climate sensitivity. *Geophysical Research Letters*, *48*(4), e2020GL089609. https://doi.org/10.1029/2020gl089609

Seeley, J. T., & Wordsworth, R. D. (2021). Episodic deluges in simulated hothouse climates. *Nature*, *599*(7883), 74–79. https://doi.org/10.1038/s41586-021-03919-z

Shellito, C. J., Lamarque, J.-F., & Sloan, L. C. (2009). Early Eocene Arctic climate sensitivity to pCO2 and basin geography. *Geophysical Research Letters*, *36*(9). https://doi.org/10.1029/2009gl037248

Siler, N., Roe, G. H., & Armour, K. C. (2018). Insights into the zonal-mean response of the hydrologic cycle to global warming from a diffusive energy balance model. *Journal of Climate*, *31*(18), 7481–7493. https://doi.org/10.1175/jcli-d-18-0081.1

Siler, N., Roe, G. H., Armour, K. C., & Feldl, N. (2019). Revisiting the surface-energy-flux perspective on the sensitivity of global precipitation to climate change. *Climate Dynamics*, *52*(7–8), 3983–3995. https://doi.org/10.1007/s00382-018-4359-0

Stephens, G. L., & Ellis, T. D. (2008). Controls of global-mean precipitation increases in global warming GCM experiments. *Journal of Climate*, *21*(23), 6141–6155. https://doi.org/10.1175/2008jcli2144.1

Takahashi, K. (2009). The global hydrological cycle and atmospheric shortwave absorption in climate models under CO2 forcing. *Journal of Climate*, *22*(21), 5667–5675. https://doi.org/10.1175/2009jcli2674.1

Trenberth, K. E. (1998). Atmospheric moisture residence times and cycling: Implications for rainfall rates and climate change. *Climatic Change*, *39*(4), 667–694. https://doi.org/10.1023/a:1005319109110

Vecchi, G. A., & Soden, B. J. (2007). Global warming and the weakening of the tropical circulation. *Journal of Climate*, *20*(17), 4316–4340. https://doi.org/10.1175/jcli4258.1

Wolf, E., Haqq-Misra, J., & Toon, O. (2018). Evaluating climate sensitivity to CO2 across Earth's history. *Journal of Geophysical Research: Atmospheres*, *123*(21), 11–861. https://doi.org/10.1029/2018jd029262

Wolf, E., & Toon, O. (2013). Hospitable Archean climates simulated by a general circulation model. *Astrobiology*, *13*(7), 656–673. https://doi.org/10.1089/ast.2012.0936

Yang, J., Leconte, J., Wolf, E. T., Goldblatt, C., Feldl, N., Merlis, T., et al. (2016). Differences in water vapor radiative transfer among 1D models can significantly affect the inner edge of the habitable zone. *The Astrophysical Journal*, *826*(2), 222. https://doi.org/10.3847/0004-637x/826/2/222

Zachos, J. C., Dickens, G. R., & Zeebe, R. E. (2008). An early Cenozoic perspective on greenhouse warming and carbon-cycle dynamics. *Nature*, *451*(7176), 279–283. https://doi.org/10.1038/nature06588

Zhu, J., & Poulsen, C. (2020a). On the increase of climate sensitivity and cloud feedback with warming in the Community Atmosphere Models. [Dataset] (Vol. *47*). Retrieved from https://doi.org/10.5281/zenodo.12631679. *Zenodo*.(18)

Zhu, J., & Poulsen, C. J. (2020b). On the increase of climate sensitivity and cloud feedback with warming in the community atmosphere models. *Geophysical Research Letters*, *47*(18), e2020GL089143. https://doi.org/10.1029/2020gl089143

Zhu, J., Poulsen, C. J., & Otto-Bliesner, B. L. (2024). Modeling past hothouse climates as a means for assessing earth system models and improving the understanding of warm climates. *Annual Review of Earth and Planetary Sciences*, *52*(1), 351–378. https://doi.org/10.1146/annurev-earth-032320-100333